

TABLE OF CONTENTS

Section	Page	
I. INTRODUCTION	1	1/A9
II. BACKGROUND	2	1/A10
III. LPE GROWTH STUDIES	3	1/A11
A. Methods of Growth	3	1/A11
B. Liquid-Solid Composition Studies	5	1/A13
C. Morphology	9	1/B4
IV. InGaAsP EVALUATION	12	1/B7
A. Multiple-Layer Structure	12	1/B7
B. X-Ray Lattice Parameter Measurements	15	1/B10
C. Layer Uniformity	20	1/C1
V. DEVICE FABRICATION AND PROPERTIES	25	1/C6
A. Broad-Area Devices	25	1/C6
B. Oxide-Stripe Devices	32	1/C13
VI. CONCLUSIONS	37	1/D4
REFERENCES	39	1/D6

830-H-14

MAY 2

NAS1-26: 3268

NASA Contractor Report 3268

COMPLETED

ORIGINAL

Study of LPE Methods for Growth of InGaAsP/InP CW Lasers

I. Ladany, F. Z. Hawrylo,
R. T. Smith, and E. R. Levin

CONTRACT NAS1-15440
APRIL 1980

NASA

47

NASA Contractor Report 3268

Study of LPE Methods for Growth of InGaAsP/InP CW Lasers

I. Ladany, F. Z. Hawrylo,
R. T. Smith, and E. R. Levin
RCA Laboratories
Princeton, New Jersey

Prepared for
Langley Research Center
under Contract NAS1-15440



National Aeronautics
and Space Administration

Scientific and Technical
Information Office

1980

PREFACE

This Final Report covers work performed at RCA Laboratories during the period August 3, 1978 to July 2, 1979 under Contract No. NAS1-15440. The Laboratory Director was B. Hershenov, the Group Head was M. E. Ettenberg, and the Project Scientist was I. Ladany. The COTR was H. Hendricks, NASA Langley Research Center, Hampton, Virginia.

Staff members and support personnel who contributed to this work in addition to the authors, and the area of their contributions are listed below.

J. K. Butler*	-	Far-field radiation theory
E. P. Bertin**	-	EPMA
N. DiGiuseppe	-	Photoluminescence
T. Furman	-	LPE growth
D. Gilbert	-	Device measurements
M. Harvey	-	Device fabrication
H. Kowger	-	Device fabrication
R. Paff	-	X-ray diffraction

*Consultant; permanent address: Department of Electrical Engineering, Southern Methodist University, Dallas, TX.
**Member Technical Staff.

SUMMARY

Two methods for liquid-phase growth of InGaAsP/InP lasers have been studied. Single-phase growth, based on saturated melts and 5°C supercooling, was compared to two-phase growth using excess InP and 20°C nominal supercooling. Substrates cut on the (100) plane were used, and morphology in both cases was excellent and comparable to that obtainable in AlGaAs materials. A high degree of reproducibility was obtained in the material grown by the two-phase method, which is therefore presently preferred for the preparation of laser material. A refractive index step of 0.28 and an index $n = 3.46$ were obtained for $\text{In}_{.81}\text{Ga}_{.19}\text{As}_{.5}\text{P}_{.5}$ lasing at 1.3 μm . The temperature dependence of threshold current was found to follow $\exp(T/60 \text{ K})$, in contrast to $\exp(T/120 \text{ K})$ typical of AlGaAs lasers. Devices fabricated in this program show a large dependence of the threshold current on cavity length and very little dependence on cavity thickness over the 0.2- to 0.4- μm range. Oxide-stripe lasers with typical room-temperature cw threshold currents of 180 mA were obtained and some of them showed single-mode behavior without lateral cavity modifications. Continuous operation of 800 h at room temperature has been obtained so far without noticeable degradation.

TABLE OF CONTENTS

Section	Page
I. INTRODUCTION	1
II. BACKGROUND	2
III. LPE GROWTH STUDIES	3
A. Methods of Growth	3
B. Liquid-Solid Composition Studies	5
C. Morphology	9
IV. InGaAsP EVALUATION	12
A. Multiple-Layer Structure	12
B. X-Ray Lattice Parameter Measurements	15
C. Layer Uniformity	20
V. DEVICE FABRICATION AND PROPERTIES	25
A. Broad-Area Devices	25
B. Oxide-Stripe Devices	32
VI. CONCLUSIONS	37
REFERENCES	39

LIST OF ILLUSTRATIONS

Figure	Page
1. Temperature measurement in single-phase growth	4
2. Comparison of two LPE growth methods used during this program	5
3. Liquid-solid composition plot for LPE growth by the two-phase method. Growth temperature was 631°C	8
4. Reproducibility of five runs using the same melt composition and growth schedule. Growth temperature was 635°C	9
5. Upper: surface appearance of a multiple-layer LPE structure grown by the two-phase method. Lower: image of a fiber-coupled diode reflected from a group of single-phase-grown wafers	10
6. Photomicrograph of a cleaved and stained cross section of a typical laser structure	12
7. Comparison of SEM with angle-lapped-optical photo- micrograph	13
8. Angle-lapped cross section showing severe material faults introduced due to improper melt composition	14
9. Cross sections and angle laps of high-quality LPE material	15
10. Intensity contribution of various layers in x-ray diffraction from multiple-layer InGaAsP/InP material ...	17
11. X-ray diffraction profiles of InGaAsP/InP material in normal and Berg-Barrett reflection	19
12. Photoluminescence spectra at two positions ~0.5 cm apart on the quaternary surface of typical laser material. The curves are shifted vertically by an arbitrary amount	20

LIST OF ILLUSTRATIONS (Continued)

Figure	Page
13. EDXRA scans of two different regions of a quaternary epitaxial layer	23
14. Threshold dependence on temperature for an InGaAsP/InP laser	28
15. Far-field beam pattern in the transverse direction. Points are obtained by measurement, and solid lines are the result of computations based on the three-slab waveguide model applied to this device	29
16. Threshold current dependence on cavity length for a series of sawed-side lasers	33
17. Output power vs current plot for a cw InGaAsP/InP laser operated at 23°C	33
18. Output spectrum of the laser used in the previous figure	34
19. Power-current plot for presently fabricated oxide-stripe InGaAsP/InP lasers	35
20. Lifetest data of two lasers, representative of devices developed in this program	36

I. INTRODUCTION

In future large space structures (LSST) and fast computer-to-computer applications there exists the need for good data-transfer systems. As the advantages of silica optical fibers become widely recognized, the value of devising optical systems capable of operating at wavelengths near $1.3\text{ }\mu\text{m}$ becomes increasingly clear. In particular, certain satellite applications of interest to NASA require fiber systems (LSST-Electronic Mail Satellite) that are resistant to radiation; at the operating wavelength of conventional (AlGaAs) lasers ($0.82\text{ }\mu\text{m}$), optical fibers suffer increased attenuation when exposed to moderate radiation levels (LSST environment of 10^7 rads for a lifetime of 10 to 30 years). However, at longer wavelengths ($\lambda \geq 1.0\text{ }\mu\text{m}$) the effect of radiation on silica fibers is dramatically reduced. Moreover, reduced fiber scattering losses (due to λ^{-4} dependence of Rayleigh scattering) provide significantly less signal attenuation at 1.3 than at $0.82\text{ }\mu\text{m}$. Finally, pulse dispersion due to the wavelength dependence of the refractive index is close to zero for most practical fibers at a wavelength near 1.27 to $1.3\text{ }\mu\text{m}$. For these reasons, InGaAsP/InP heterojunction structures capable of providing both optical sources and detectors near $1.3\text{ }\mu\text{m}$ are needed to satisfy NASA data systems requirements.

RCA Laboratories has for several years supported various programs aimed at developing such structures both by vapor-phase epitaxy (VPE) and by liquid-phase epitaxy (LPE). More recently increased emphasis has been placed on LPE. The present report covers work done under NASA sponsorship, for the period from 3 August 1978 to 2 July 1979 in developing cw lasers emitting near $1.3\text{ }\mu\text{m}$, using the LPE process.

II. BACKGROUND

A crucial difference between the InGaAsP system and the previously studied AlGaAs system is that the quaternary system is not automatically lattice-matched for all compositions. It is well established, through considerable work at RCA Laboratories [1] that a close degree of lattice match is essential for the achievement of low-threshold reliable lasing action. The main reasons for this situation are that a good lattice match is necessary to prevent the introduction and growth of dislocation networks which affect reliability, and that excessive lattice mismatch causes nonradiative centers to be accumulated at the heterojunction boundaries, resulting in reduced efficiency and high threshold current densities. It is becoming clearer, on the basis of recent work, that the mechanism by which dislocations move from the heterojunctions into the active region involve stress which is often caused by lattice mismatch. It is also possible, and the evidence for this is increasing, that stress on the order of 2×10^8 dynes/cm² or larger causes nonradiative centers to be generated even if they are not present originally [2]. Apart from these considerations, close lattice match is also required to obtain smooth layers, free from voids and other disturbances affecting device operation. Thus the achievement of lattice-matched growth assumes the first priority in any InGaAsP development program. We have therefore devoted a considerable portion of our effort to the study of melt compositions, growth processes, and the resultant solid compositions. In the next section we describe our growth-oriented studies and the conclusions reached, and in subsequent sections we discuss devices and measurement results obtained on them.

1. G. H. Olsen, C. J. Nuese, and M. Ettenberg, IEEE J. Quantum Electron. QE-15, 688 (1979).
2. I. Ladany, T. R. Furman, and D. P. Marinelli, Electron. Lett. 15, 342 (1979).

III. LPE GROWTH STUDIES

A. METHODS OF GROWTH

A variety of techniques have been described in the literature for LPE growth of InGaAsP. The first to result in good quaternary lasers was the one described by Hsieh [3], who used a supercooling method with exact equilibrium composition melts. We have followed this procedure in what we call single-phase growth which is carried out as follows. The melt components are carefully weighed and heated to a temperature at which an exactly saturated melt is obtained. Then the melt is cooled by a fixed step, thus producing a supercooled melt, and then brought in contact with an InP substrate where rapid precipitation and growth takes place. The crucial element in this process is believed to be the degree of supercooling, because it provides a large driving force for crystal growth. Without supercooling, a melt may in fact dissolve the substrate rather than grow a layer.

A large part of the effort in single-phase growth is of necessity devoted to the establishment of exactly saturated melt compositions. Unfortunately, the results of one laboratory are not easily used by another because the exact temperature and thermal gradients in one furnace seldom match those of another.

For the purpose of establishing melt compositions, we have studied the melt appearance at elevated temperatures by observation through the walls of a semitransparent gold reflector furnace. In addition we probed each melt using a moveable thermocouple probe as shown in Fig. 1. One of the problems with single-phase growth is that there is a continued loss of phosphorus in the furnace due to its high vapor pressure over the solution. Consequently, it is necessary to add some excess InP to

3. J. J. Hsieh, Appl. Phys. Lett. 28, 283 (1976).

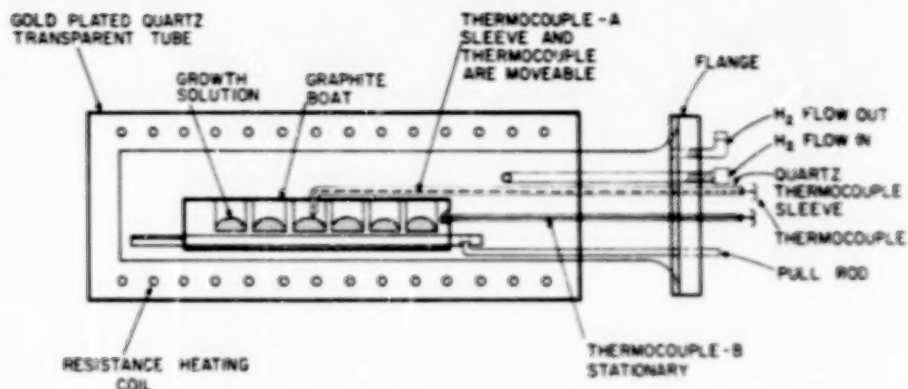


Figure 1. Temperature measurement in single-phase growth.

the melt, and in general there is a tendency for the previous history of the melt to affect the exact composition. A relatively large degree of supercooling is employed, however, to overcome minor alterations in the solution composition.

The other growth process is called two-phase growth [4,5] because in addition to the solution, a solid InP phase in the shape of platelets is maintained on the solution surface. This second technique has the advantage of automatically compensating for the phosphorus loss, thus assuring that the solution is maintained at equilibrium. A disadvantage of two-phase growth is that it is not possible to achieve the same degree of supercooling, since some of the growth occurs onto the InP material introduced into the melt. Supercooling in this type of growth occurs because only upper portions of the melt interact with the InP platelets in the time allowed by the furnace cooling rate. The main features of these two schemes are illustrated in Fig. 2. It may be noted that because of the difference in the degree of

4. T. Yamamoto, K. Sakai, S. Akiba, and Y. Suematsu, IEEE J. Quantum Electron. QE-14, 95 (1978).
5. R. E. Nahory and M. A. Pollack, Electron. Lett. 14, 727 (1978) and M. A. Pollack, R. E. Nahory, J. C. DeWinter, and A. A. Ballman, Appl. Phys. Lett. 33, 314 (1978).

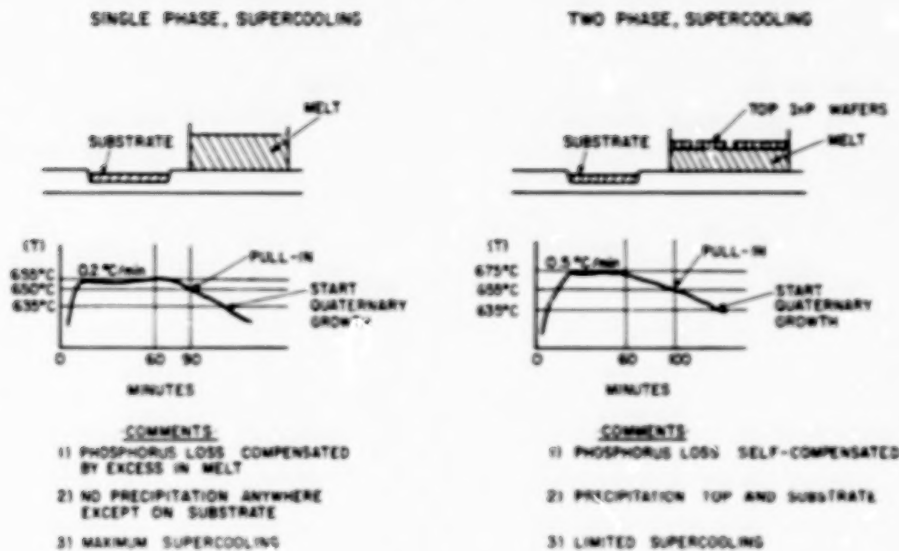


Figure 2. Comparison of two LPE growth methods used during this program.

supercooling allowed by the two processes, we use a larger Δt for the two-phase growth.

Both growth systems have yielded laser material which was processed into cw lasers, and there appears to be little difference between them as far as device properties are concerned. However, threshold current densities in our two-phase growth are somewhat lower, and reproducibility is better so that the material to follow, unless specifically mentioned, will apply to devices grown by the two-phase method.

B. LIQUID-SOLID COMPOSITION STUDIES

Most of our solid analyses were made in an indirect way. The composition and various properties of quaternary InGaAsP material are related in a relatively simple way and can be derived from the known

values of the ternary or binary material. Moon et al. [6] have obtained interpolation formulas for the lattice spacing and for the bandgap, in terms of x and y where x denotes the mole fraction of As in the quaternary, and y denotes the mole fraction of Ga.

$$a_0(\text{\AA}) = 5.8694 + 0.1887x - 0.4184y + 0.0137xy \quad (1)^*$$

$$E_g(\text{eV}) = 1.35 - x + 1.4y - 0.33xy - (0.758 - 0.28x)y(1-y) \\ - (0.101 + 0.109y)x(1-x) \quad (2)$$

These equations can be used to generate values of the lattice constant a_0 and the bandgap E_g for different x and y values, from which the quaternary layer composition corresponding to a given E_g and a_0 can be determined.

Our layers were evaluated by measuring lattice constants using precision x-ray diffractometry and by measuring bandgaps from the photoluminescence peak. We have also compared the values of one sample with results obtained by direct analysis using EPMA (Electron Probe Micro-Analysis) as shown below:

Derived Composition	In. _{.68} Ga. _{.32} As. _{.64} P. _{.36}
EPMA Composition	In. _{.70} Ga. _{.30} As. _{.66} P. _{.34}

We consider this agreement satisfactory in view of the limited accuracy of EPMA under ideal conditions, and the special difficulties in the present case due to the fractional micron layers available for analysis.** This is not to say that x-ray diffractometry of a number of layers at one time is easy, but as will appear in a later section, we have succeeded in unravelling the multiple reflections and assigning the various x-ray diffraction peaks to the proper layers.

6. R. L. Moon, G. A. Antypas, and L. W. James, J. Electron. Mater. 3, 625 (1974).

*Eq. (1) is a slightly modified form due to G. H. Olsen.

**X-ray lattice constant values have not been corrected for strain, to yield free-crystal lattice constants. This correction becomes negligible as the lattice match condition is approached.

In order to study the growth parameters and the resultant solid, we have found it very convenient to use a special diagram, Fig. 3. The scales on this plot were carefully chosen so that the melt composition and the resultant solid composition can be displayed together, but shifted laterally by a small amount. For the melt we plot the gallium and the arsenic content only, since the melt consists of a sea of indium in which the other elements can be treated as impurities, and since the phosphorus concentration is automatically maintained at the liquid-solid equilibrium value by the excess InP. Furthermore, because only two elements completely specify the solid (because of stoichiometry) and only two elements need be specified for the liquid, we obtain a symmetrical and relatively simple diagram which fully covers the melt composition and the corresponding solid composition. Referring to Fig. 3, we show such a plot for growth at 631°C. The scales on the left side of the figure apply to the liquid and those toward the right refer to the solid. The points labeled A to F refer to melt compositions used and the same letters primed show the resultant solid compositions. Also shown are lines of constant lattice mismatch including the line for zero mismatch, and lines of constant bandgap (expressed in wavelength units). It can be seen how changing the liquid composition leads to corresponding changes in the solid. The point labeled C is an example which does not fit the general trend and is taken to represent an error of some unknown type. From the position of the other solid points it is possible to construct a melt composition line giving the best predicted compositions for growing lattice-matched layers of various bandgaps at 631°C. It may also be pointed out that a lattice mismatch of up to $\sim 0.30\%$ yields high-quality laser material without visible flaws or other effects associated with excessive mismatch.

Figure 4 shows a similar plot where we display the reproducibility in growth for a group of five runs all having the same melt composition.

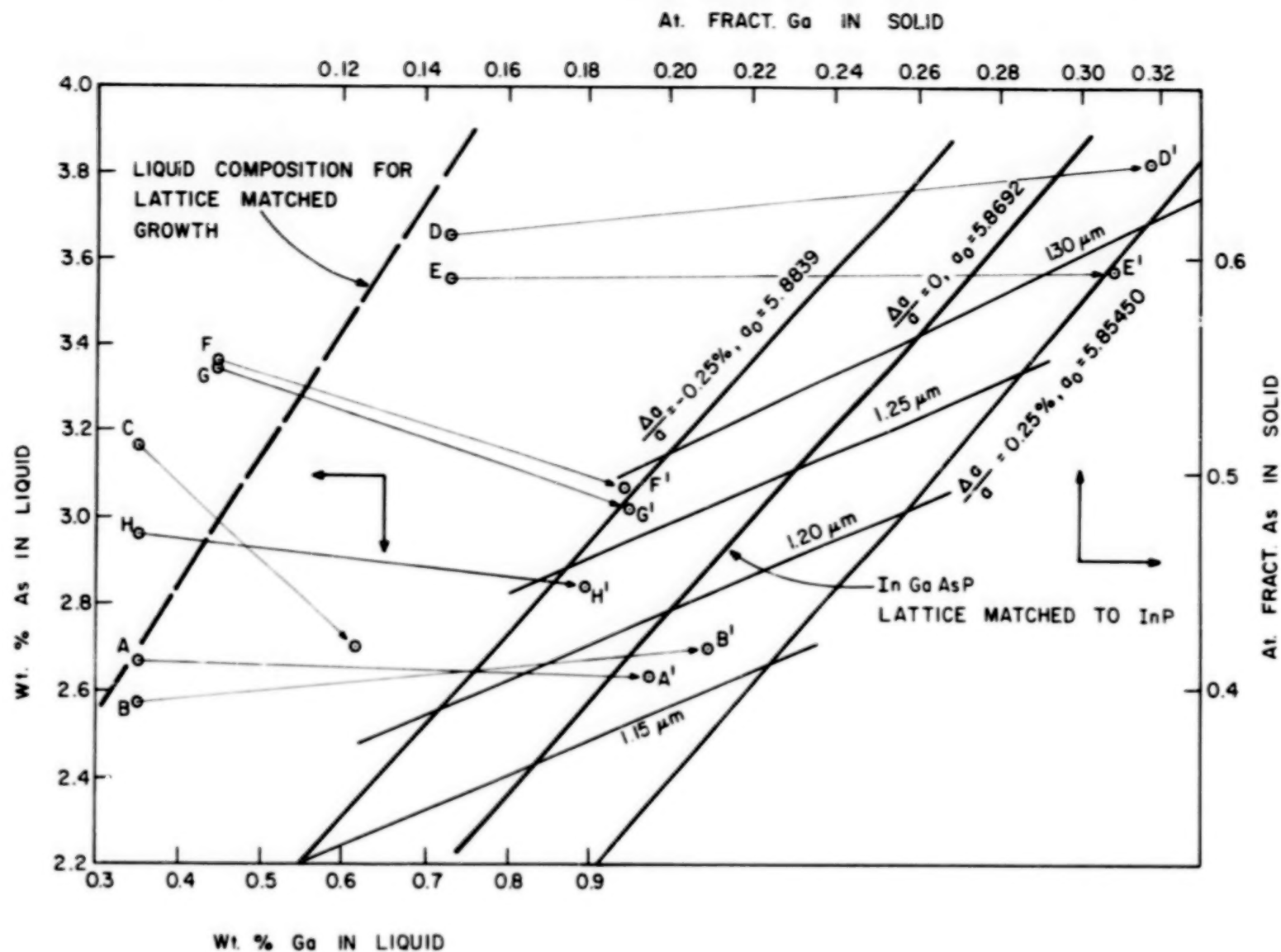


Figure 3. Liquid-solid composition plot for LPE growth by the two-phase method. Growth temperature was 631°C.

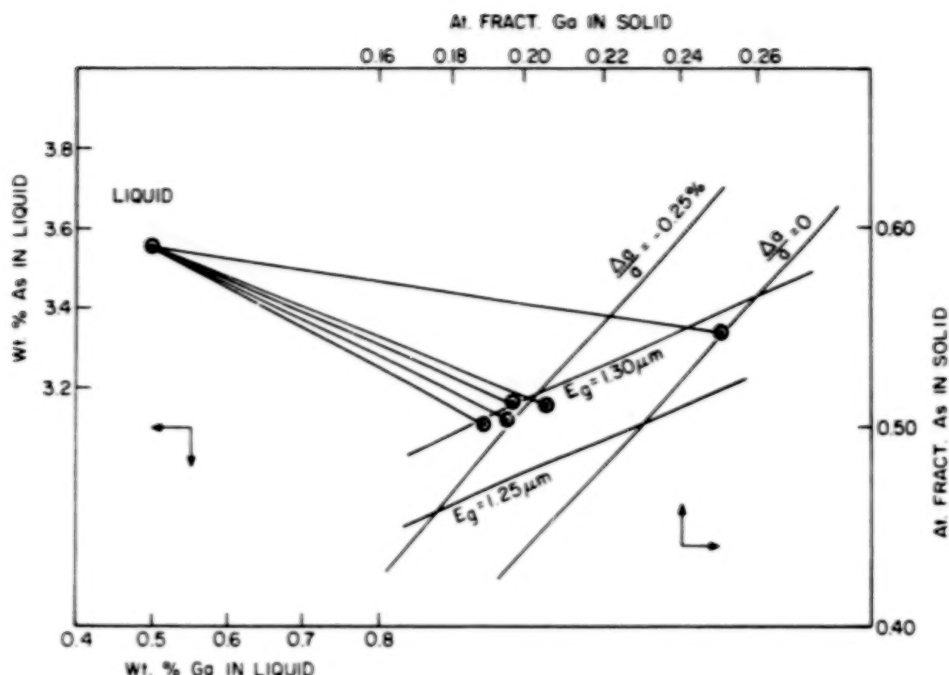


Figure 4. Reproducibility of five runs using the same melt composition and growth schedule. Growth temperature was 635°C.

The resultant distribution in solid composition for four of the runs shows a range of 0.19 to 0.21 atom fraction Ga and a range of 0.5 to 0.51 atom fraction As. The lattice mismatch from InP, indicated in %, ranged from -0.20 to -0.28 for four of the runs, and was equal to -0.03 for the fifth. The variation in bandgap was 1.29 to 1.30 μm . The material reproducibility demonstrated here appears to be satisfactory.

C. MORPHOLOGY

All of our growth was made on the (100) plane of Sn-doped InP substrates with etch-pit densities of 10^4 to 10^5 cm^{-2} . As long as the lattice mismatch did not exceed 0.3 to 0.4%, the morphology of the materials was generally equivalent to that obtained in the AlGaAs/GaAs system. This is illustrated in Fig. 5 where the upper part shows a

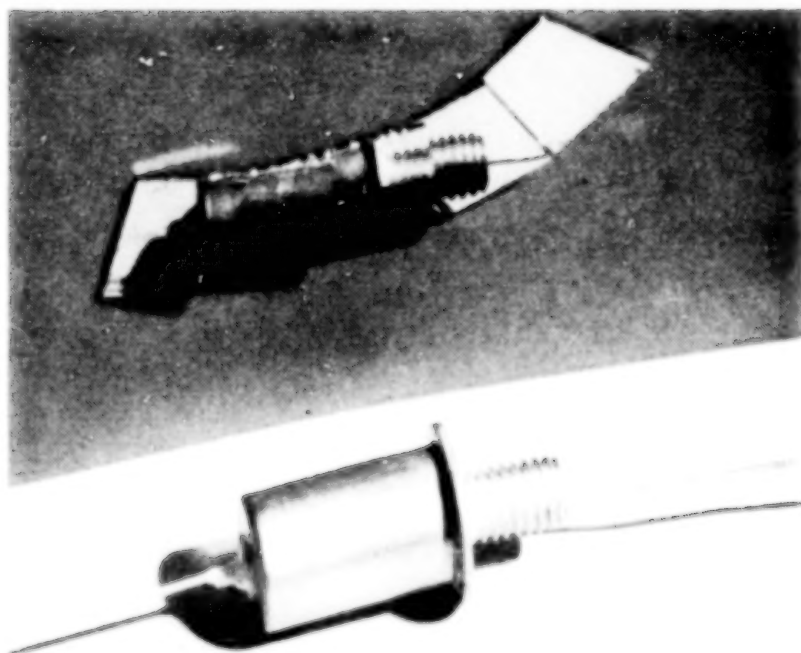
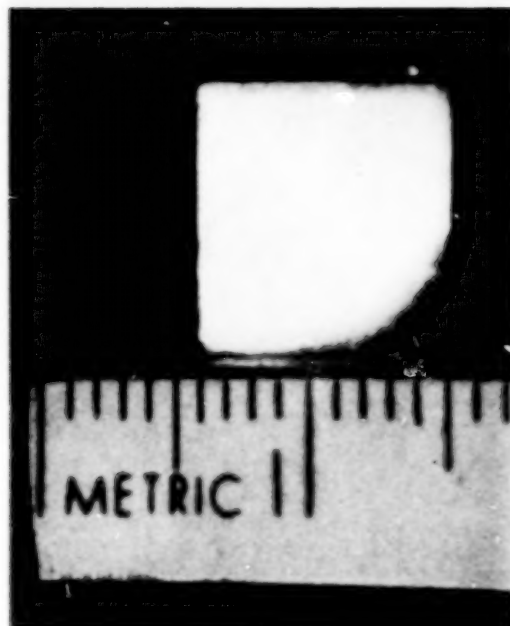


Figure 5. Upper: surface appearance of a multiple-layer LPE structure grown by the two-phase method. Lower: image of a fiber-coupled diode reflected from a group of single-phase-grown wafers.

macrophotograph of a completed wafer grown by the two-phase method. Toward the right edge of the wafer, one can discern faint contour lines characteristic of LPE in general. The bottom part of the figure shows the image of a fiber-coupled laser reflected from a group of quaternary wafers grown by the single-phase method.

IV. InGaAsP EVALUATION

A. MULTIPLE-LAYER STRUCTURE

A typical structure grown during this program is shown in Fig. 6. An n-type InP layer is first grown onto the substrate, followed by a quaternary cavity layer, a p-type InP layer and another quaternary layer used to facilitate contacting. The bandgap of the cap layer is made slightly larger ($\sim 1.2 \mu\text{m}$) in order to reduce absorption of laser light spreading into the cap.

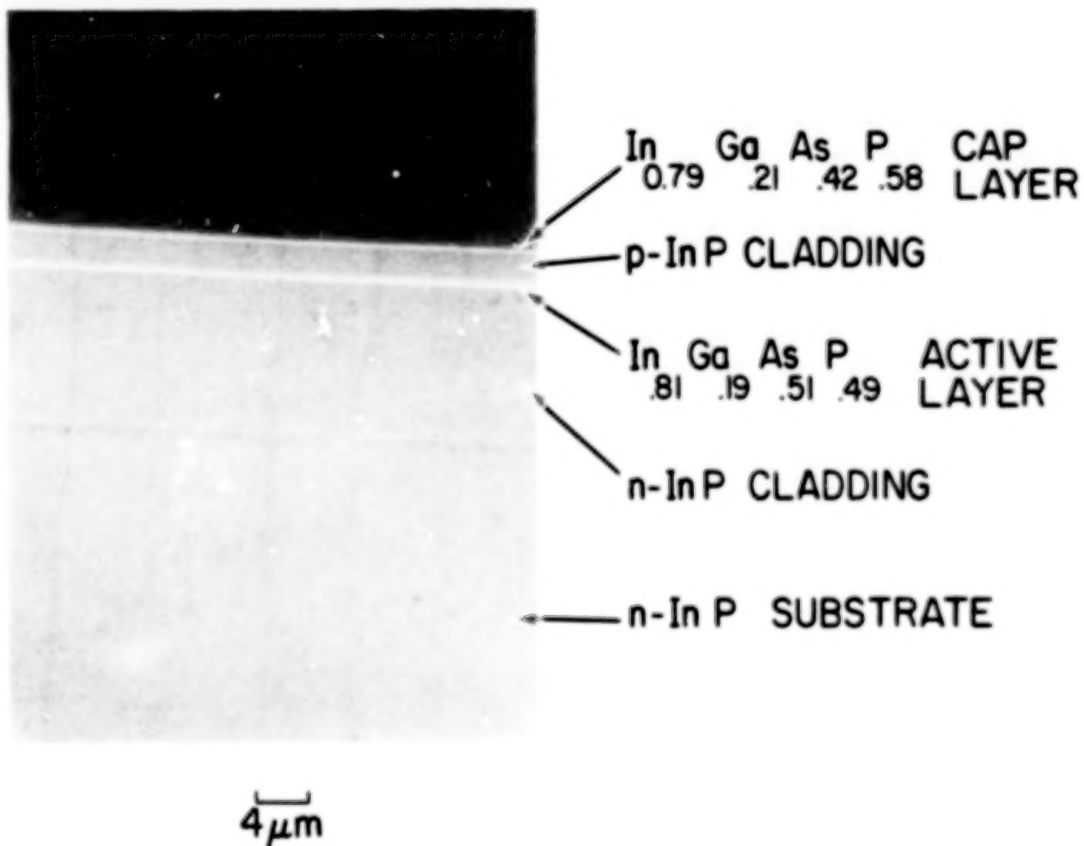


Figure 6. Photomicrograph of a cleaved and stained cross section of a typical laser structure.

Figure 7 shows a comparison of the cross section of a laser structure as observed in the SEM and in an optical photomicrograph of an angle-lapped section. The SEM provides the most accurate thickness for an individual device, while the value of the angle lap is that details of the structure can be examined over distances comparable to those used in a typical diode. The few bumps visible in Fig. 7 are not significant from the point of view of device performance, but the

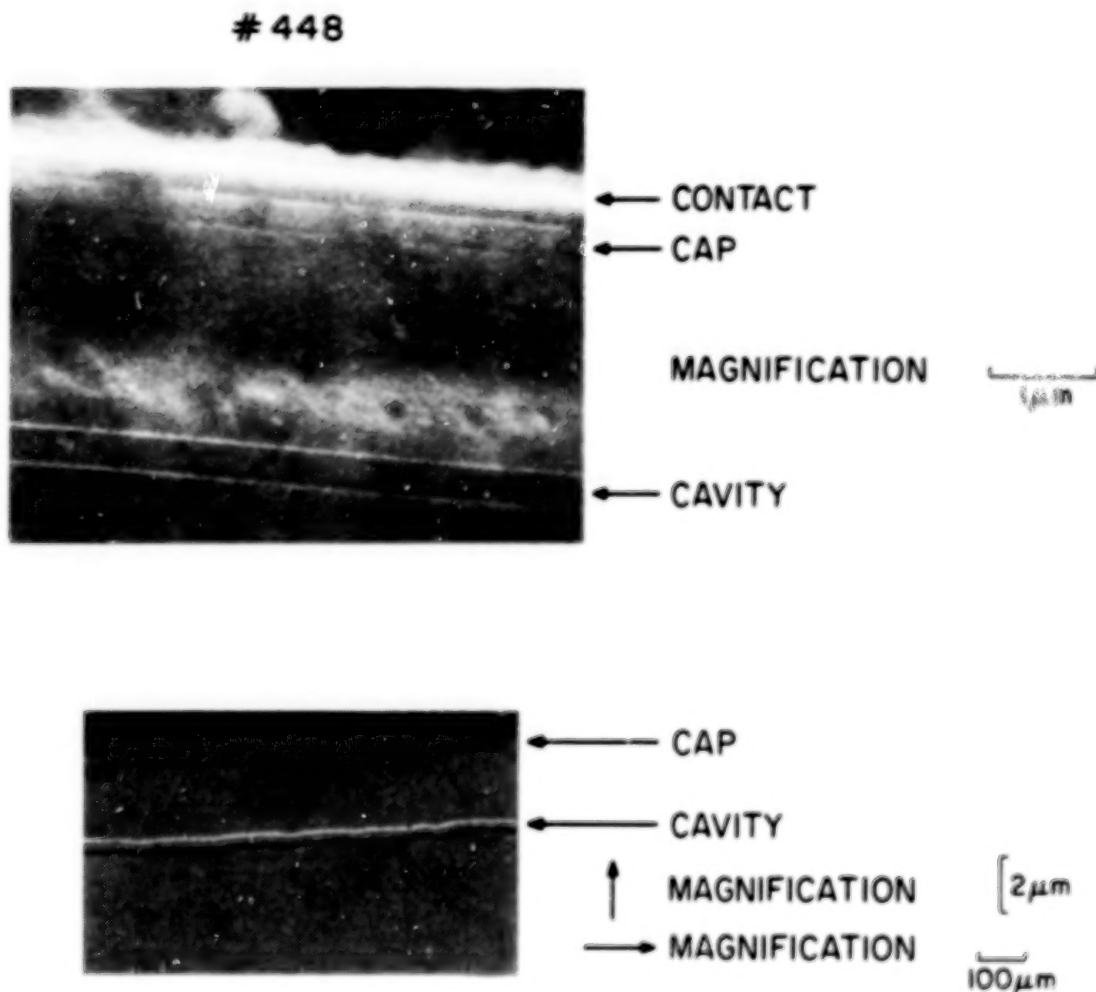


Figure 7. Comparison of SEM with angle-lapped-optical photomicrograph.

flaws visible near the right edge or the flaws shown in Fig. 8 definitely are. Typical cross sections and angle laps for good material having active layer thicknesses of 0.2 and 0.4 μm are shown in Fig. 9.

#424

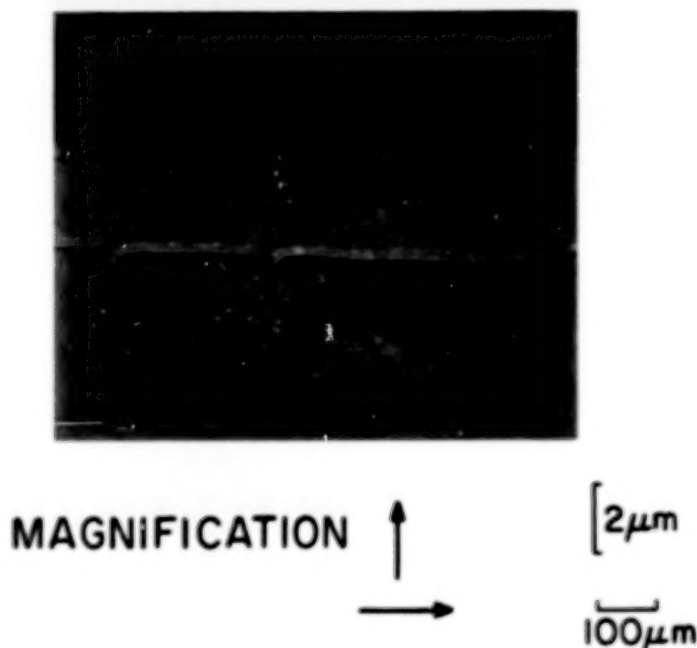


Figure 8. Angle-lapped cross section showing severe material faults introduced due to improper melt composition.

As mentioned before, our standard method of analyzing solid compositions is to take x-ray diffraction measurements on a complete structure, and from this obtain lattice constants for the two quaternary layers. In some of the grown material we have found anomalous diffraction patterns, which seem to occur only when certain abnormal melts are used. In the next section we discuss these particular results and our general x-ray diffraction measurements in more detail.

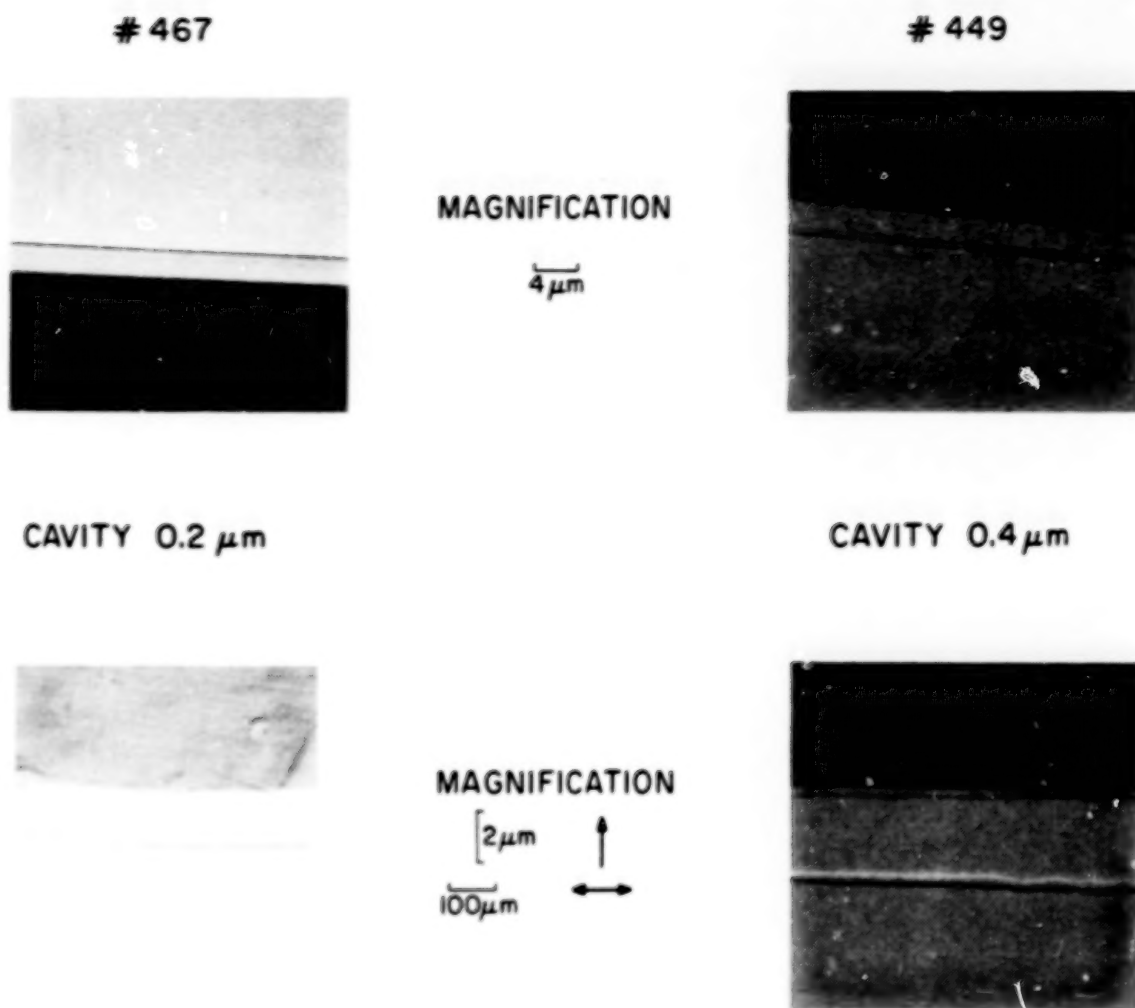


Figure 9. Cross sections and angle laps of high-quality LPE material.

B. X-RAY LATTICE MEASUREMENTS

X-ray diffractometry measurements have been routinely employed to determine the lattice mismatch $[\Delta a/a = (a_{\text{InP}} - a_Q)/a_{\text{InP}}]$ of $\text{In}_{1-y}\text{Ga}_y\text{As}_x\text{P}_{1-x}$ quaternary alloys of the 4-layer laser structure. The ability of the technique to detect a lattice mismatch of the quaternary cap, Q_1 , and cavity, Q_2 , is dependent on the choice of radiation, layer thickness, choice of diffraction geometry, and instrumental resolution limit.

The resolution limit of the instrument used in this analysis is $\Delta a/a \sim 3 \times 10^{-4}$. For the typical layer thicknesses encountered, Cu $K\alpha_1$ - $K\alpha_2$ 400 and 440 reflections from the (100) material have been found to supplement each other and provide satisfactory sensitivity. The fractional intensity contribution of each of the layers can be approximated by evaluating the expression $I/I_0 = 1 - \exp[-\mu t(\csc[\theta - \phi] + \csc[\theta + \phi])]$ where μ is the linear absorption coefficient, t is the layer thickness, θ is the Bragg angle of the chosen reflecting plane, and ϕ is the angle that the plane makes with respect to the (100) specimen surface. For the 400-Cu $K\alpha_1$ reflection ($\mu \sim 1173 \text{ cm}^{-1}$; $\theta \sim 31.67^\circ$; and $\phi = 0^\circ$) this expression is evaluated and plotted as a function of t in Fig. 10. Although infinite penetration depth (corresponding to 99% absorption) is $10.3 \mu\text{m}$, it can be seen that 80% of the diffracted intensity is obtained from the first $3.6 \mu\text{m}$ of beam penetration. The quaternary cap and cavity contribute 8.6% and 3.2%, respectively. Thus, the 400-Cu $K\alpha_1$ reflection provides sufficient sensitivity to enable detection of both cap and cavity. One might ask how it is possible to differentiate cap from cavity without selective etch removal of the cap. This problem is particularly severe if the lattice mismatch of either is less than the resolution limit, and/or if there exist compositional gradients, and/or if the layer thicknesses are not known. Berg-Barrett geometry then provides supplemental information because it limits penetration depth. Using a 440-Cu $K\alpha_1$ reflection in Berg-Barrett geometry ($\mu \sim 1173 \text{ cm}^{-1}$; $\theta \sim 47.93^\circ$; and $\phi_{100-440} = 45^\circ$), an infinite penetration depth of only $2.0 \mu\text{m}$ is attained. Thus for a 4-layer structure of typical dimensions only the quaternary cap and p-InP will contribute to the diffraction event.

Turning now to a discussion of x-ray anomalies, we have found peculiar diffraction patterns for some solid compositions grown at 635°C . A structure which was carefully analyzed had the dimensions given in Table 1.

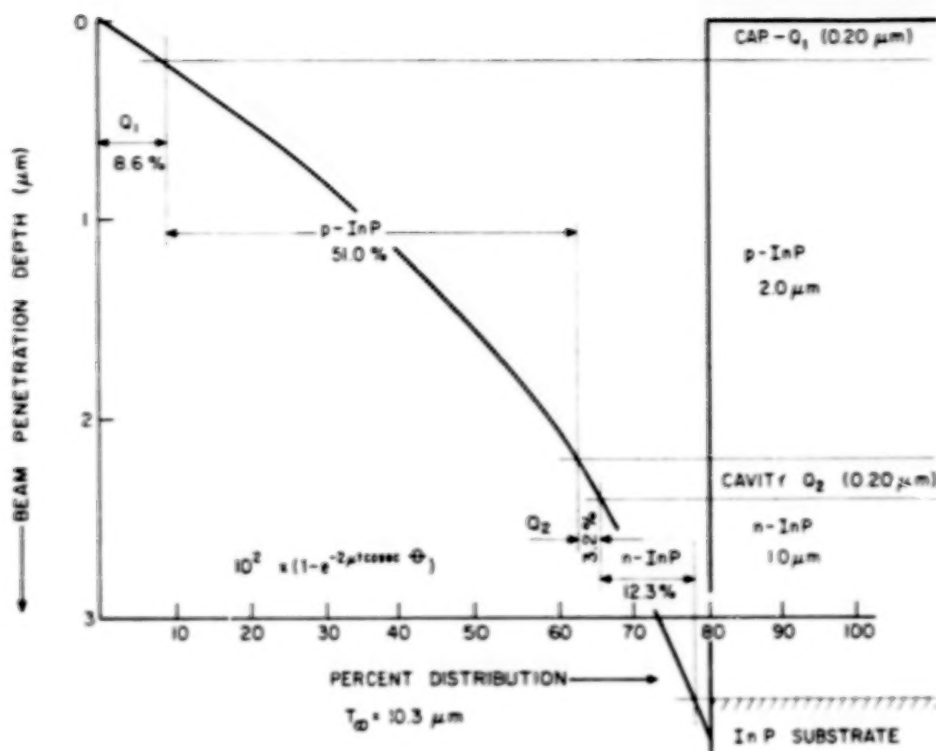


Figure 10. Intensity contribution of various layers in x-ray diffraction from multiple-layer InGaAsP/InP material.

TABLE 1. DIMENSIONS OF STRUCTURE USED IN DETAILED X-RAY ANALYSIS

Type of layer	Thickness (μm)
Quaternary Cap, Q_1	0.4
p-InP Cladding	1.8
Quaternary Cavity, Q_2	0.4

In order to resolve the patterns, two sets of x-ray data were taken, the first on the entire structure and the second after the top quaternary layer Q_1 and part of the p-InP cladding layer were etched off.

X-ray diffraction profiles of normal 400- and 440- $\text{CuK}\alpha_1$ Berg-Barrett reflections in before- and after-etch states are shown in Fig. 11. If only the quaternary cap and cavity were mismatched from InP, only three phases would be obtained in the before-etch 400- $\text{CuK}\alpha_1$ - α_2 diffraction profile shown in the upper left of Fig. 11; however, in addition to these three phases an additional phase (shaded) is observed. As can be seen in the before-etch 400- and 440- $\text{CuK}\alpha_1$ - α_2 diffraction profiles shown on the top of Fig. 11, the cap comprises two very slightly mismatched phases, and does not appear in the after-etch cases shown at the bottom. Cross-sectional optical examination of this sample after-etch shows that not only was the 0.4- μm cap removed, but also 0.2 μm of the initially 1.8- μm -thick p-InP layer was removed. It should be noted that in agreement with this observation, the after-etch diffraction profiles show not only the absence of any contribution from the cap, but also a slight reduction of the contribution from the p-InP in the after-etch 400- $\text{CuK}\alpha_1$ - α_2 profile. Additional evidence of a p-InP mismatch is obtained by comparing the $\Delta a/a$ range calculated for the cap from splittings observed in the 400 and 440 diffraction profiles. In the Berg-Barrett 440 case, an infinite penetration depth of 2.0 μm is attained, and thus only the 0.4- μm cap and 1.8- μm cavity are sampled. The lattice mismatch of cap and p-InP based on the 440 splitting does not correlate with that calculated for the cap and InP splitting of the 400 diffraction profile. It does, however, correlate with the mismatch calculated from the splitting of cap and shaded (p-InP) peaks of the 400 diffraction profile. A comparison of calculated and observed intensities of the phases observed in the 400 before-etch diffraction profile provides yet another argument for a mismatch of the p-InP. The intensity contributed by the shaded peak is much greater than that calculated for the 0.4- μm cap (16%) or 0.4- μm cavity (6%). It is, however, in better agreement with that calculated for the 1.8- μm p-InP (46%).

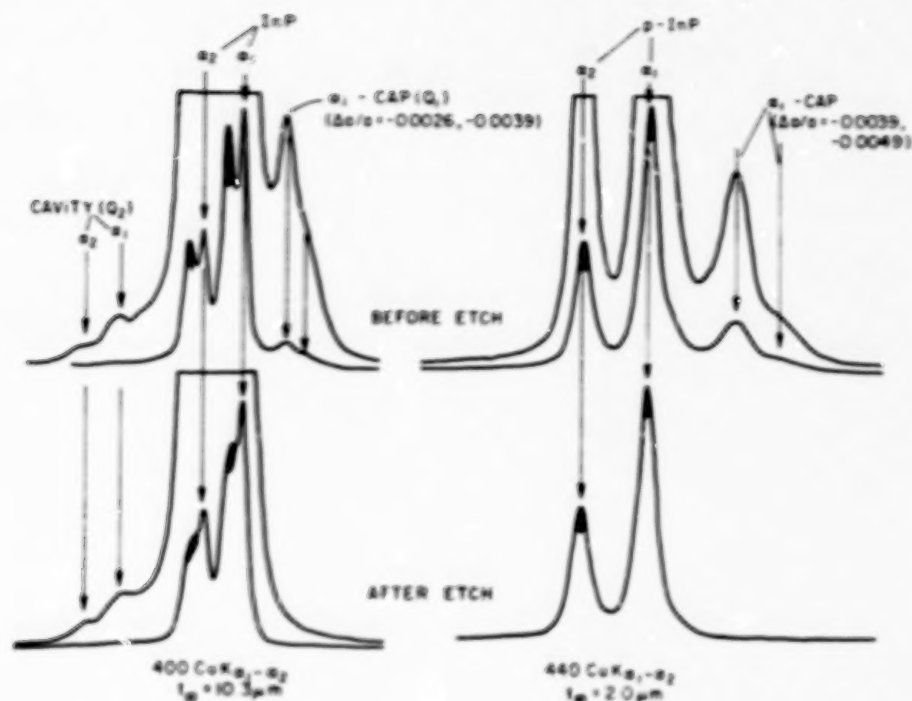


Figure 11. X-ray diffraction profiles of InGaAsP/InP material in normal and Berg-Barrett reflection.

In summary, results of comparisons of (1) x-ray diffraction profiles obtained in before- and after-etch sample states, (2) lattice mismatches calculated from normal 400 and 440 Berg-Barrett reflections in the before-etch sample state, and (3) observed and calculated intensities of the 400 before-etch reflection are consistent with a lattice mismatch of the nominal p-InP relative to n-type bulk InP. This phenomenon has been most consistently observed in LPE-grown structures having a quaternary cavity in tension ($\Delta a/a > 0$) and has not been observed for LPE structures having a cavity in compression ($\Delta a/a < 0$). The source of this mismatch (i.e., stress or compositional variations) is currently being studied.

C. LAYER UNIFORMITY

1. Photoluminescence Analysis

One important question relating to quaternary growth is the uniformity of the layers grown. We have attempted to evaluate this in two ways. First we took photoluminescence (PL) spectra on two different spots ~ 0.5 cm apart on the surface of a typical InGaAsP laser wafer. The resultant spectra are shown in Fig. 12. It can be seen that the spectral peak is similar in the two cases, indicating the top quaternary layer has the same E_g . This test, however, does not pinpoint the composition or the lattice constant.

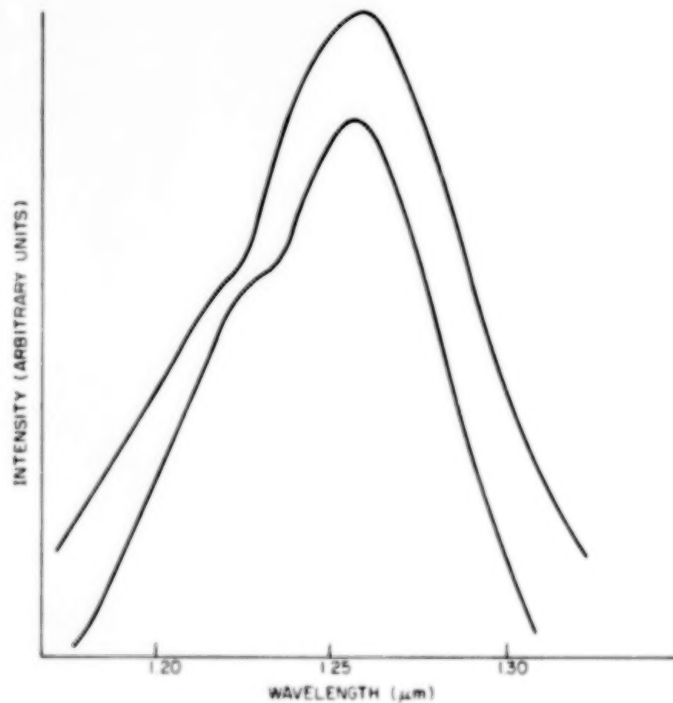


Figure 12. Photoluminescence spectra at two positions ~ 0.5 cm apart on the quaternary surface of typical laser material. The curves are shifted vertically by an arbitrary amount.

A different approach to the problem of assessing uniformity was taken by using Energy Dispersive X-ray Analysis, the results of which will be discussed next.

2. Energy Dispersive X-Ray Analysis

Quantitative and semi-quantitative compositional studies of a thin LPE layer of $\text{In}_{1-y}\text{Ga}_y\text{As}_x\text{P}_{1-x}$ on InP substrate were carried out by Energy Dispersive X-Ray Analysis (EDXRA) in the scanning electron microscope. The layer was about 4000 Å thick and had a nominal composition of $(1-y) = 0.7$, $x = 0.6$. Determinations of composition at a number of points on the layer were made by EDXRA and compared with results obtained by electron probe microanalysis (EPMA).^{*} Results obtained by the two methods are compared in Table 2. The data are in good overall agreement; however, there is some divergence of the values for As and P. While both of these methods have been successful in treating the III-V alloy system and are subject to some of the same uncertainties, the EPMA data here are considered to be the more reliable because of more favorable experimental and statistical factors.

TABLE 2. COMPARISON OF COMPOSITION AS DETERMINED BY ELECTRON PROBE MICROANALYSIS AND ENERGY-DISPERSIVE X-RAY ANALYSIS OF 4000-Å-THICK $\text{In}_{1-y}\text{Ga}_y\text{As}_x\text{P}_{1-x}$ LAYER

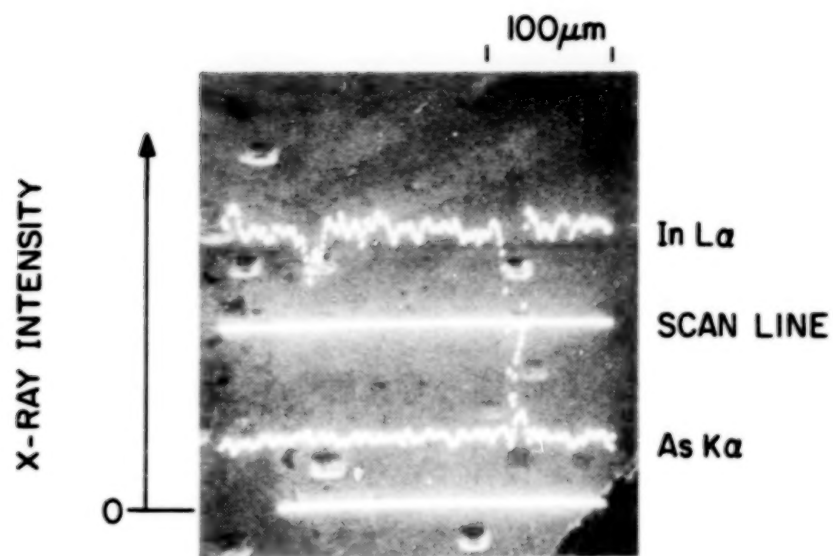
<u>Nominal</u>	<u>EPMA</u>	<u>EDXRA</u>
In(1-y) 0.7	0.70	0.76
Ga(y) 0.3	0.30	0.31
As(x) 0.6	0.66	0.68
P(1-x) 0.4	0.34	0.31

^{*}By E. P. Bertin, RCA Laboratories.

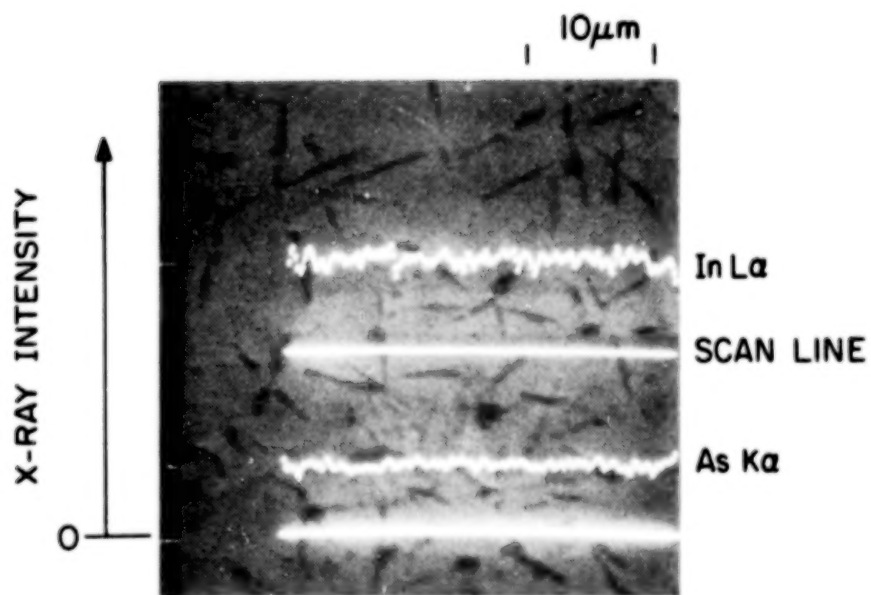
In addition to the point-by-point determination of composition, the uniformity of the layer was investigated by the use of the line profile analysis (LPA) mode of EDXRA operation. In the LPA technique, the intensity of a preselected x-ray peak (or several different peaks) is recorded as a function of the position of the exciting electron beam, thus yielding an indication of changes of composition within the specimen. Figure 13(a) shows LPA traces obtained for the $L\alpha$ radiation of In and the $K\alpha$ radiation of As. The profiles are superimposed on an SEM image of the InGaAsP layer, so that a direct correlation of the x-ray intensities with physical features of the layer can be made readily. The surface is seen to contain a number of pits, at which the x-ray intensities vary sharply. Outside these pits, on the "normal" region of the surface, the x-ray intensities are constant: deviations of the traces from the (constant) average values are relatively small and represent statistical fluctuations in x-ray emission and detection. The statistical nature of the fluctuations, which are usually encountered in this kind of analysis, has been confirmed by comparisons of LPAs repeated along the same scan line and by observation of profiles obtained at different locations.

Figure 13(b) shows typical In $L\alpha$ and As $K\alpha$ line profiles obtained on the same layer at higher magnification. In this case, as in Fig. 13(a), the x-ray intensities are constant, i.e., do not vary with the position of the exciting electron beam. Although some surface features (not studied in detail) are present, the x-ray intensities apparently are not much affected by them.

Line profile analyses utilizing the Ga $K\alpha$ and P $K\alpha$ characteristic x-rays yielded completely similar results: that is, except at obvious surface defects, there was no variation of the intensity of emitted x-rays with position on the layer. It may thus be concluded that the composition of the LPE quaternary layer is constant; no local or long-range fluctuations in In:Ga or As:P ratio were detected.



(a)



(b)

Figure 13. EDXRA scans of two different regions of a quaternary epitaxial layer.

The minimum change in composition detectable in this line scan method is estimated to be on the order of 5 to 10% of the mean composition.

The abrupt changes in In and As x-ray intensities at the pit of Fig. 13(a) indicate that the EDXRA LPA technique is indeed sufficiently sensitive to reveal changes in relative composition. While the altered geometry of x-ray emission and collection at the pit position precludes the drawing of firm conclusions, the line scans of Fig. 13(a) suggest that, at the defect, the In concentration is lower and the As concentration is higher than in "normal" regions of the LPE layer.

The results of these PL and EDXRA examinations provide an indication that the composition of the material along the junction plane shows no drastic jumps or variations.

V. DEVICE FABRICATION AND PROPERTIES

Two types of devices were fabricated under this program. The first is a broad-area sawed-side structure using Sn-Au contacts on the n side and plated Ni-Au contacts on the p side. This structure is suitable for making threshold current-density measurements, length-dependence studies, cavity-thickness measurements, and far-field beam diameter studies.

The other structure is an oxide-stripe laser configuration similar to that used in the AlGaAs system. The main difference in our fabrication of stripe lasers is that we use Au-Zn contacts on the p side instead of plated contacts. By this means we obtain the necessary high doping on the p side without having to resort to a separate diffusion step. As will be discussed later, stripe devices made in this way have very good characteristics, particularly in regard to threshold current, and thermal resistance. In any case, a diffusion step can always be added should this prove to be advantageous.

In the next section we discuss device results obtained on broad-area devices.

A. BROAD-AREA DEVICES

Table 3 shows a summary of measurements on a series of wafers grown in this program. These runs were selected because they represent material grown with the intention of meeting criteria in regard to threshold, cavity width, and wavelength. Exploratory or experimental runs, where modifications were introduced deliberately in order to study the system and its response to perturbations, were excluded from this listing. It appears from the table that wavelength control is very good, but that threshold control shows some fluctuations. Part of this may be due to our method of threshold determination, using sawed-side laser chips. As discussed in a later section, the length of the laser may

in some cases exert considerable influence on the threshold-current density, a subject we intend to explore in the future.

TABLE 3. SUMMARY OF WAFERS GROWN DURING PROGRAM

RUN No.	d (μm)	L (μm)	J_{th} (kA/cm^2)	PL/EL (μm)	R_{th} ($^{\circ}\text{C}/\text{W}$)
438	0.2	305	2.7	1.29	
441	0.2	386	6.0	1.29	
444	0.23	244	1.5	1.30	32*
447	0.23	361	2.4	1.30	
448	0.42	305	2.4	1.30	19.5†
449	0.40	284	3.1	1.30	
455	0.25	467	3.5	1.34	
460	0.23	284	2.6	1.29	
463	0.3	445	4.7	1.32	
469	0.24	386	1.5	1.32	

*Measured on a sawed-side device.

†Measured on an oxide-stripe device.

Thermal resistance values, although not as low as the best obtained in AlGaAs diodes, are adequate for good cw performance. The biggest contribution to the thermal resistance arises in the quaternary cap layer, InP having a thermal conductivity ($0.8 \text{ W cm}^{-1} ^{\circ}\text{C}^{-1}$) [7] which is higher than that of GaAs. Ultimately, this layer may be omitted

7. Chemical Rubber Company, Handbook of Chemistry and Physics, 1977-1978 edition.

entirely, although at present we believe its advantages in contact-processing outweigh the disadvantage of higher thermal resistance.

The cavity thickness d varies between 0.2 and 0.4 μm , and there appears to be little if any correlation between d and the threshold current density.

1. Temperature Dependence of the Threshold Current

Figure 14 shows the measured dependence of the threshold current as a function of device temperature. Using the usual exponential relation to describe this dependence, we obtain a value for θ of 60 K. Another way of representing the temperature dependence is by means of an exponential power function, also shown in the figure. The main contribution to the temperature dependence comes from bandgap step at the heterojunctions which for this material is typically 0.35 eV, again comparable to that in AlGaAs devices. It is therefore difficult to see why the temperature dependence in quaternary materials should be so much greater, viz., $\theta = 60$ K as compared to 120 K for AlGaAs. It has been suggested that this may be a consequence of defects at the heterojunctions [8].

2. Refractive Index and Beam-Pattern Measurements*

The far-field beam pattern in a direction normal to the junction plane, called the transverse beam pattern, provides useful information about the refractive index step on the two sides of the cavity. A study of this pattern shows to what extent existing theory, developed for the AlGaAs system applies to the quaternary system, and provides a measurement of the refractive index step, the absolute value of the index, and the index dispersion.

8. M. Ettenberg, C. J. Nuese, and H. Kressel, J. Appl. Phys. 50, 2949 (1979).

*These measurements were made on an oxide-stripe cw device.

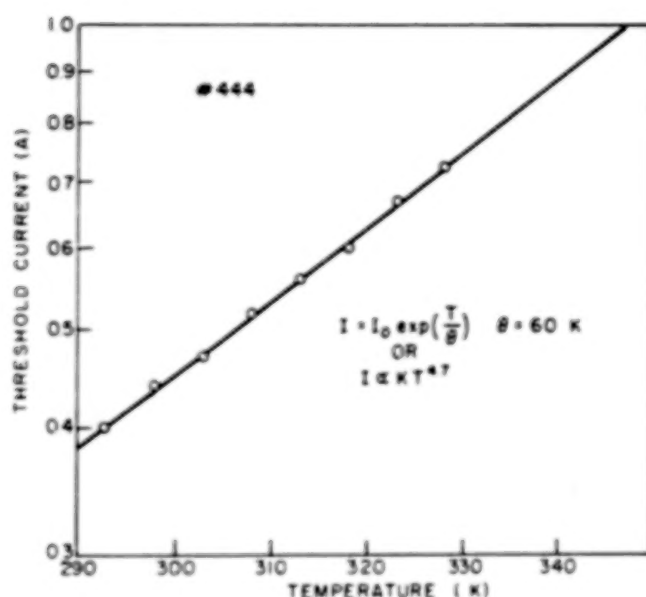


Figure 14. Threshold dependence on temperature for an InGaAsP/InP laser.

Figure 15 shows a plot of the computed beam pattern* using the three-slab waveguide model as presented in Kressel and Butler [9]. The points are taken from the measured beam for an InGaAsP laser. The experimental pattern was normalized at the peak, but otherwise no curve-fitting was employed. It is seen that the agreement with an index step Δn of between 0.25 and 0.30 is very good. We take the best fit to occur for $\Delta n = 0.28$. Table 4 shows the assumptions and results of this analysis. From the known refractive index of InP at $1.27 \mu\text{m}$ of 3.2, we obtain an index of 3.48 for $\text{In}_{.81}\text{Ga}_{.19}\text{As}_{.5}\text{P}_{.5}$ at $1.27 \mu\text{m}$.

9. H. Kressel and J. K. Butler, Semiconductor Lasers and Heterojunction LED's (Academic Press, New York, 1977).

*We are indebted to J. K. Butler for carrying out the theoretical beam-pattern calculation.

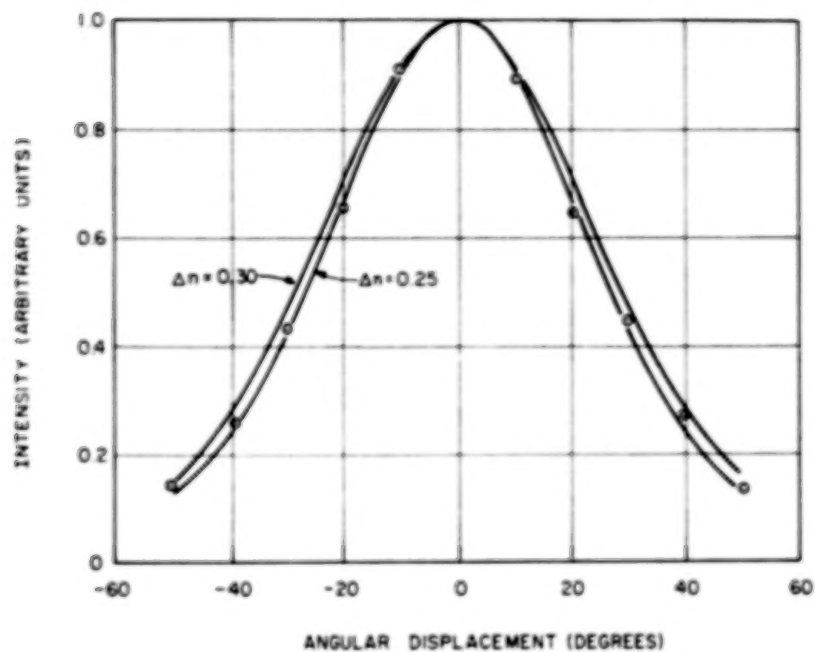


Figure 15. Far-field beam pattern in the transverse direction. Points are obtained by measurement, and solid lines are the result of computations based on the three-slab waveguide model applied to this device.

TABLE 4. REFRACTIVE INDEX CALCULATION

n_{InP} at $1.27 \mu\text{m}$	$= 3.2$
d	$= 0.34 \mu\text{m}$
λ	$= 1.27 \mu\text{m}$

n_1	InP
n_3	$\text{In}_{.81}\text{Ga}_{.19}\text{As}_{0.5}\text{P}_{0.5}$
n_5	InP

For $\Delta n = 0.28$, $n_3 = 3.48$

The mode spacing of this laser was measured to be 6.05 \AA and was used to compute the effective cavity index n_e through

$$\Delta\lambda = \frac{\lambda^2}{2L n_e} \quad (3)$$

giving $n_e = 4.83$.

The effective index is related to the actual index n_3 and the index dispersion by

$$n_e = n_3 \left(1 - \frac{\lambda}{n_3} \frac{dn}{d\lambda} \right) \quad (4)$$

from which we obtain for the index dispersion of this material near $1.27 \text{ }\mu\text{m}$

$$\frac{dn}{d\lambda} = -1.0/\mu\text{m} \quad (5)$$

The index of $\text{In}_{.81}\text{Ga}_{.19}\text{As}_{.5}\text{P}_{.5}$ at its bandgap wavelength of $1.3 \text{ }\mu\text{m}$ is then calculated to be 3.46.

Since the geometrical index dispersion [9] has been neglected in this calculation, we consider the agreement with the index calculated by G. H. Olsen et al. ($n = 3.5$) [10] from binary values to be satisfactory.

3. Threshold Relations

The basic form of laser formulas relating various parameters to threshold current density are well known. However, D. Botez [11] of RCA Laboratories has recently succeeded in deriving a particularly simple form of this relation, where all parameters are included explicitly, without reference to tables or graphs of the confinement

10. G. H. Olsen, C. J. Nuese, and M. Ettenberg, Appl. Phys. Lett. 34, 262 (1979).

11. D. Botez, Appl. Phys. Lett. 35, 57 (1979).

factor. As this equation is so convenient, we briefly indicate its origin, and then use it to discuss InGaAsP laser parameters.

The standard threshold formula is given by

$$J_{th} = \frac{1}{\eta\beta} \left[\alpha_o d + \frac{d}{\Gamma} G_{th} \right] \quad (6)$$

$$G_{th} = \alpha_i + \frac{1}{L} \ln 1/R \quad (7)$$

Here η is the laser internal efficiency at threshold, Γ is the confinement factor, G_{th} is the mode gain at threshold, α_i is the internal cavity loss, L is the cavity length, $R = \sqrt{R_1 R_2}$ is the geometrical mean of the two facet reflectivities, and β and α_o are parameters expressing the linear dependence of the gain g on the current density J through

$$g = \beta \frac{\eta J}{d} - \alpha_o \quad (8)$$

Botez has shown that Γ can be represented in closed form as

$$\Gamma \approx \frac{D^2}{2+D^2}; \quad D = \frac{2\pi d}{\lambda^2} \sqrt{n_1^2 - n_2^2} \quad (9)$$

so that the explicit threshold formula becomes

$$J_{th} = \frac{1}{\eta\beta} \left[d(\alpha_o + G_{th}) + \frac{1}{d} \frac{\lambda^2 G_{th}}{2\pi^2(n_1^2 - n_2^2)} \right] \quad (10)$$

which emphasizes the dependence on d , the cavity thickness or

$$J_{th} = \frac{d}{\eta\beta} \left\{ \alpha_o + \alpha_i + \frac{\Omega}{d^2} + \frac{1}{L} \left[\left(1 + \frac{\Omega}{d^2} \right) \ln 1/R \right] \right\} \quad (11)$$

$$\Omega = \frac{\lambda^2}{2\pi^2(n_1^2 - n_2^2)}$$

which emphasizes the dependence on length. Botez has fitted Eq. (10) to the data of Nahory and Pollack [5], assuming that a linear gain-current relationship holds. From this he has obtained a value $\alpha_0 = 35 \text{ cm}^{-1}$ which is much different from the value obtained for AlGaAs, $\alpha_0 = 215 \text{ cm}^{-1}$.

A consequence of this difference is that the threshold dependence on cavity thickness is flatter than in the ternary system. In other words, one does not expect the device to be sensitive to cavity thickness in the 0.1- to 0.4- μm range (except for very short diodes). Our data given in Table 3 agree with this conclusion as no influence of d on the threshold current density is in evidence.

One series of experiments was made with material of somewhat high threshold to determine the effect of cavity length on the threshold current density. The results are displayed in Fig. 16. One can see that by fitting such data to Eq. (11), various laser parameters can be extracted. It is, however, undesirable to do this at the present time, because the material tested was not representative of currently produced lower threshold devices and because the scatter of the data was large. However, the large slope of this curve is revealing, for it shows that the longer the device, the lower the threshold current density. To be sure, this has also been observed in AlGaAs, but there the effect is not of such magnitude. This very large dependence on cavity length is again a consequence of the small α_0 value, so that our data support the previously made observations. It is clear from these arguments that InGaAsP/InP lasers should be made with longer cavities than similar AlGaAs devices (alternately they would benefit from having end losses reduced by reflecting mirrors).

B. OXIDE-STRIPE DEVICES

An optical power vs current plot of a stripe laser is shown in Fig. 17. The spectrum of this device was recorded at a 4-mW output

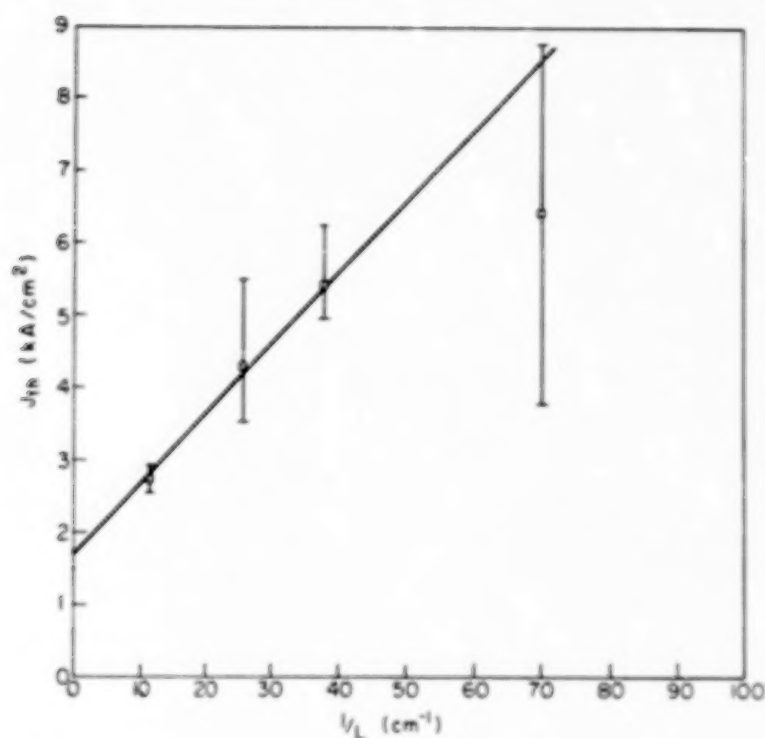


Figure 16. Threshold current dependence on cavity length for a series of sawed-side lasers.

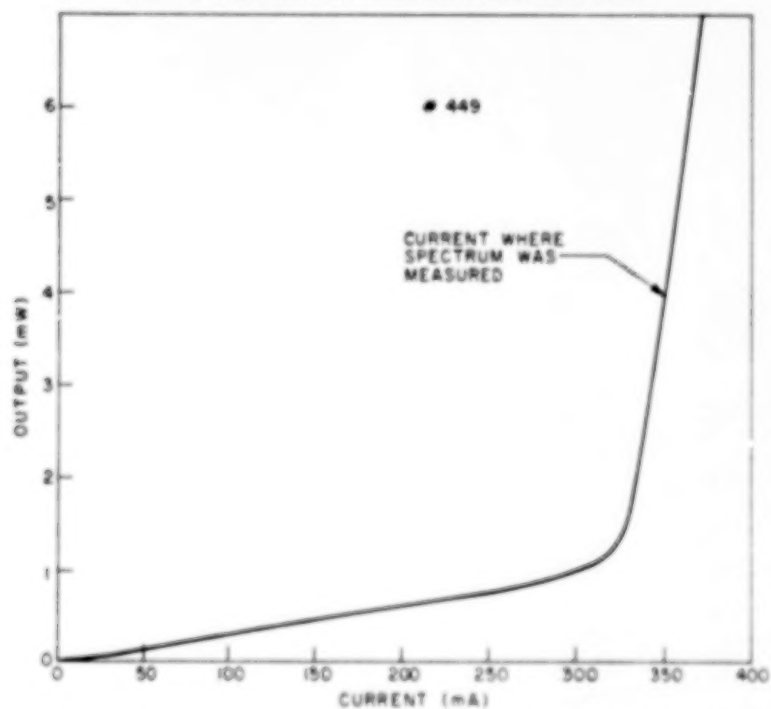


Figure 17. Output power vs current plot for a c-InGaAsP/InP laser operated at 23°C.

value and is shown in Fig. 18. As reported recently by Olsen et al. [10] for the case of VPE lasers, there is a similar tendency for LPE material to show single-mode behavior. However, this only occurs occasionally, and then only for a limited current range, and cannot therefore form the basis for a useful single-mode device. Rather, we conclude that, perhaps because of the longer wavelength relative to the cavity dimensions, quaternary structures may be more easily fabricated into single-mode lasers using appropriate sidewall boundaries.

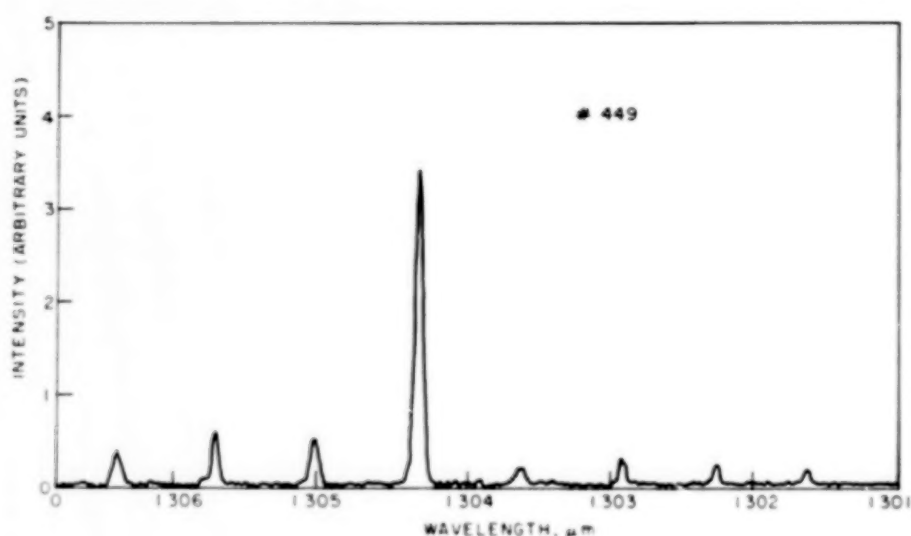


Figure 18. Output spectrum of the laser used in the previous figure.

The threshold current density in the previous device was rather high, but this is not too surprising in view of the 3.1-kA/cm^2 threshold current density for the broad-area devices made from this material.

A typical power curve for a lower threshold material is shown in Fig. 19 with a threshold current of 180 mA. The high degree of linearity is also noteworthy. Two such units have been put on lifetest and have so far accumulated 350 and 800 hours, as shown in Fig. 20. The

operating output power is also indicated. Although we cannot tell how these devices will continue to perform, the behavior indicated so far is similar to that shown by long-life units routinely fabricated in the AlGaAs system. More units will be put on lifetest in the future in order to develop statistically significant data for these devices.

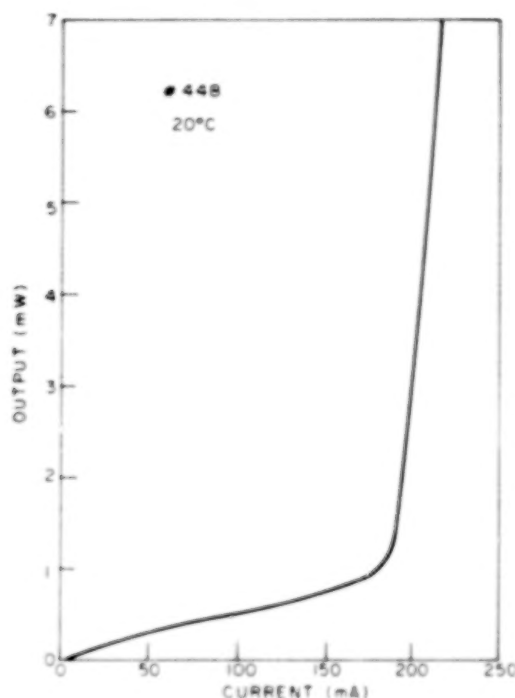


Figure 19. Power-current plot for presently fabricated oxide-stripe InGaAsP/InP lasers.

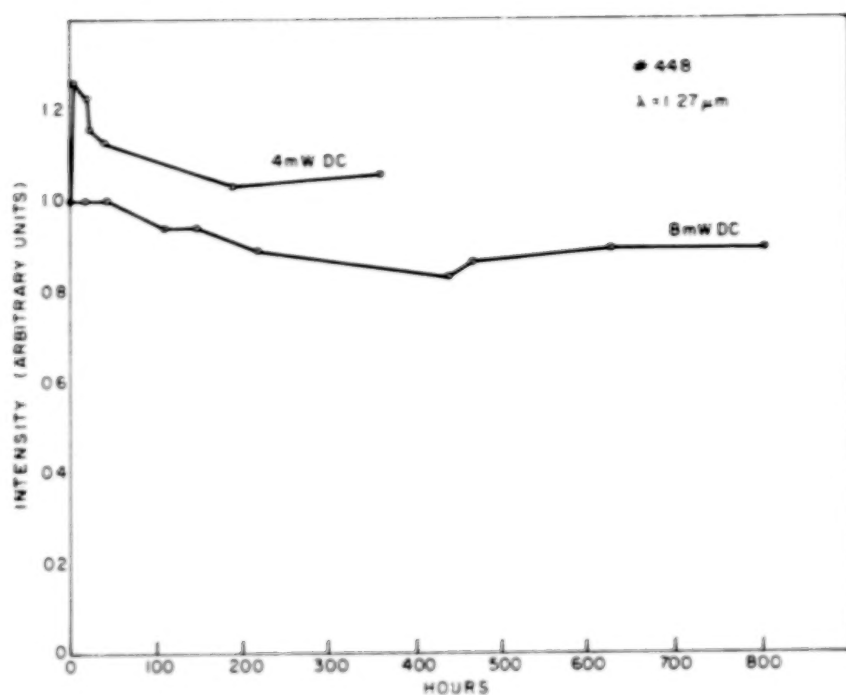


Figure 20. Lifestest data of two lasers, representative of devices developed in this program.

VI. CONCLUSIONS

Two processes were studied for the liquid epitaxial growth of InGaAsP/InP lasers emitting near 1.3 μm . The first, single-phase growth, involves use of carefully equilibrated melts and 5°C of supercooling. The second, called two-phase growth, uses excess InP in the melt and 20°C of supercooling. Both methods, applied to (100) oriented wafers, have produced cw lasers operating at room temperature with good power output and linearity. On the basis of our experience so far, two-phase growth seems to have a higher yield of low threshold material and is more reproducible. Single-phase growth may be advantageous when thicker layers are needed.

Special studies were made of the liquid and solid compositions for two-phase growth at 631 and 635°C. Reproducibility was tested in repeated runs using the same melt compositions. Wavelength and lattice constant reproducibility from run to run was excellent, while the threshold current variation was somewhat larger. Results for a series of growths are reported and tabulated.

Both broad-area sawed-side and narrow oxide-stripe lasers were fabricated. CW operation was obtained at a threshold current as low as 180 mA dc at 23°C, with no noticeable degradation in 800 h of testing accumulated so far.

The refractive index of the quaternary layer was determined from the lasing beam pattern by applying a three-slab waveguide model. The index step of the heterojunction is $\Delta n = 0.28$ from which the refractive index of $\text{In}_{.81}\text{Ga}_{.19}\text{As}_{.5}\text{P}_{.5}$ was calculated to be 3.46 at 1.30 μm .

The temperature dependence of the threshold current density was measured. Using the exponential representation, $\theta = 60$ K was obtained, indicating a significantly higher sensitivity to temperature than for comparable AlGaAs injection lasers. On the other hand, lack of sensitivity to cavity thickness and a large dependence on diode length was

observed. These latter two results indicate that α_0 , a parameter connected with the gain-current relation, is much smaller in InGaAsP than in AlGaAs devices.

Layer uniformity was assessed by means of photoluminescence and energy-dispersive x-ray analysis, and no irregularities were found within the sensitivity of the method which was estimated as 5 to 10% of the element mole fraction.

Overall, morphology of the layers and reproducibility of material properties were very good, and provide a solid foundation for the development of single-mode quaternary lasers.

REFERENCES

1. G. H. Olsen, C. J. Nuese, and M. Ettenberg, IEEE J. Quantum Electron. QE-15, 688 (1979).
2. I. Ladany, T. R. Furman, and D. P. Marinelli, Electron. Lett. 15, 342 (1979).
3. J. J. Hsieh, Appl. Phys. Lett. 28, 283 (1976).
4. T. Yamamoto, K. Sakai, S. Akiba, and Y. Suematsu, IEEE J. Quantum Electron. QE-14, 95 (1978).
5. R. E. Nahory and M. A. Pollack, Electron. Lett. 14, 727 (1978) and M. A. Pollack, R. E. Nahory, J. C. DeWinter, and A. A. Ballman, Appl. Phys. Lett. 33, 314 (1978).
6. R. L. Moon, G. A. Antypas, and L. W. James, J. Electron. Mater. 3, 625 (1974).
7. Chemical Rubber Company, Handbook of Chemistry & Physics, 1977-1978 edition.
8. M. Ettenberg, C. J. Nuese, and H. Kressel, J. Appl. Phys. 50, 2949 (1979).
9. H. Kressel and J. K. Butler, Semiconductor Lasers and Heterojunction LED's (Academic Press, New York, 1977).
10. G. H. Olsen, C. J. Nuese, and M. Ettenberg, Appl. Phys. Lett. 34, 262 (1979).
11. D. Botez, Appl. Phys. Lett. 35, 57 (1979).

1. Report No. NASA CR-3268	2. Government Accession No.	3. Recipient's Catalog No.	
4. Title and Subtitle STUDY OF LPE METHODS FOR GROWTH OF InGaAsP/InP CW LASERS		5. Report Date April 1980	
		6. Performing Organization Code	
7. Author(s) I. Ladany, F. Z. Hawrylo, R. T. Smith, and E. R. Levin		8. Performing Organization Report No. PRRL-79-CR-40	
9. Performing Organization Name and Address RCA Laboratories Princeton, New Jersey 08540		10. Work Unit No.	
		11. Contract or Grant No. NAS1-15440	
12. Sponsoring Agency Name and Address National Aeronautics and Space Administration Washington, DC 20546		13. Type of Report and Period Covered Contractor Report (8-3-78 to 7-2-79)	
		14. Sponsoring Agency Code	
15. Supplementary Notes Langley Technical Monitor: Herbert D. Hendricks Topical Report			
16. Abstract Two methods for liquid-phase growth of InGaAsP/InP lasers have been studied. Single-phase growth, based on saturated melts and 5°C supercooling, was compared to two-phase growth using excess InP and 20°C nominal supercooling. Substrates cut on the (100) plane were used, and morphology in both cases was excellent and comparable to that obtainable in AlGaAs materials. A high degree of reproducibility was obtained in the material grown by the two-phase method, which is therefore presently preferred for the preparation of laser material. A refractive index step of 0.28 and an index $n = 3.46$ were obtained for $\text{In}_{0.81}\text{Ga}_{0.19}\text{As}_{0.5}\text{P}_{0.5}$ lasing at 1.3 μm . The temperature dependence of threshold current was found to follow $\exp(T/60 \text{ K})$, in contrast to $\exp(T/120 \text{ K})$ typical of AlGaAs lasers. Devices fabricated in this program show a large dependence of the threshold current on cavity length and very little dependence on cavity thickness over the 0.2- to 0.4- μm range. Oxide-stripe lasers with typical room-temperature cw threshold currents of 180 mA were obtained and some of them showed single-mode behavior without lateral cavity modifications. Continuous operation of 800 h at room temperature has been obtained so far without noticeable degradation.			
17. Key Words (Selected by Author(s)) InGaAsP lasers LPE 1.3- μm cw lasers Quaternary III-V material Injection lasers		18. Distribution Statement Unclassified - Unlimited Subject Category 36	
19. Security Classif. (of this report) Unclassified	20. Security Classif. (of this page) Unclassified	21. No. of Pages 45	22. Price* \$4.50

*For sale by the National Technical Information Service, Springfield, Virginia 22161

END

June 30, 1981